Volume 1 | Number 1 | Jan 2013 | Pages 1–100

Journal of
Materials Chemistry A

Materials for energy and sustainability
www.rsc.org/materialsA

ROYAL SOCIETY
OF CHEMISTRY

ROYAL SOCIETY
OF CHEMISTRY

www.rsc.org/materialsA

Fe$_2$O$_3$/Cu$_2$O Heterostructured Nanocrystals

Peter Mirtchev [a], Kristine Liao [a], Elizabeth Jaluague [b], Qiao Qiao [c], Yao Tian [d], Maria Varela [c,d],

Kenneth S. Burch [e], Stephen J. Pennycook [f], Doug D. Perovic [g], Geoffrey Ozin [a,]*

a Department of Chemistry, University of Toronto, 80 St. George Street, Toronto, Ontario, Canada, M5S 3H6, Email: gozin@chem.utoronto.ca

b Department of Chemistry, Queen's University, 90 Bader Lane, Kingston, Ontario, Canada, K7L 3N6

c Departamento de Fisica Aplicada III & Instituto Pluridisciplinar, Universidad Complutense de Madrid. 28040, Madrid. Spain.

d Materials Science & Technology Division, Oak Ridge National Laboratory. Oak Ridge TN, USA, 37831

e Department of Physics, University of Toronto, 60 St. George Street, Toronto, Ontario, Canada, M5S 1A7

f Department of Materials Science and Engineering, University of Tennessee. Knoxville, TN 37996

g Department of Materials Science and Engineering, University of Toronto, 184 College Street, Toronto, Ontario, Canada, M5S 3E4

ABSTRACT

We report the synthesis of colloidal γ-Fe_2O_3/Cu_2O hetero-nanocrystals (HNCs) using a solution-phase seeded-growth approach. γ-Fe_2O_3 nanocrystals were used as seeds for the nucleation of metallic Cu followed by oxidation of the Cu domain to Cu_2O upon exposure to air. The resulting dimer, trimer, and oligomer HNCs were characterized by high resolution electron microscopy, energy dispersive X-ray spectroscopy, and powder X-ray diffraction. The iron oxide component was found to be mainly γ-Fe_2O_3 using a combination of Raman and X-ray photoelectron spectroscopy. A maximal HNC yield of 72% was achieved by reducing particle growth time to a lower growth temperature with respect to the individual component particles. Size-selective precipitation was used to enrich the nanoparticle mixture in γ-Fe_2O_3/Cu_2O dimers by removing the larger aggregates. Ultraviolet photoelectron spectroscopy was used to determine that γ-Fe_2O_3 and Cu_2O are n-doped and p-doped respectively and form a staggered, type II band alignment. As such, γ-Fe_2O_3/Cu_2O HNCs may be attractive candidates for applications in solar energy conversion and represent a valuable addition to the growing library of oxide-oxide hetero-nanocrystals.

1. INTRODUCTION

As a result of intense research interest over the last two decades, the synthesis of high-quality nanocrystalline metals, oxides, and semiconductors has progressed tremendously resulting in the promising application of these materials in the fields of optoelectronics, photovoltaics, biomedicine, and photocatalysis.[1-4] The continued requirement for materials with improved performance and multiple functionalities has shifted the focus of the field of synthetic nanochemistry to the fabrication of hybrid nanocrystals (HNCs) incorporating two or more distinct chemical domains in the same particle.[5-8] The separate components are joined though an inorganic heterojunction and can result in a variety of controlled architectures including core-shell, dimer, trimer, segmented rod, and tetrapod morphologies.[9-12] The presence of distinct domains allows HNCs to exhibit multi-dimensional functionalities such as semiconductor-metallic,[13,14] magnetic-fluorescent,[15,16] and semiconductor-insulator behaviour.[17,18] These material combinations have proven useful in manipulating photogenerated charge dynamics, catalyst recovery,[19] and increasing the chemical stability of a material without affecting its optical properties leading to higher photoluminescence quantum yields.[18,20,21] Similar tandem properties are not accessible in the corresponding single-component nanocrystals.

The majority of HNCs reported in the literature are based on transition metal chalcogenides as their syntheses are well studied and generally reproducible. Metal chalcogenides have been combined with other chalcogenides (CdSe/CdS, CdSe/ZnS, CdS/EuS)[22-24], metals (CdSe/Au)[25] and oxides (CdS/Fe_2O_3)[26-28] in a variety of architectures, and utilized in functional devices ranging from solar cells[29] to photocatalytic reactors.[30-32] However, metal chalcogenides are known to be susceptible to oxidation, photocorrosion[33], and thermal degradation which limits their performance for certain applications. Comparatively fewer reports

exist on metal oxide heterojunctions synthesized by colloidal chemistry methods.[34-37] Cao and co-workers synthesized UO_2/In_2O_3 heterodimers by high temperature solution-phase annealing of UO_2 and In_2O_3 seeds and suggested that epitaxial growth preferentially occurs at crystal facets where the first atomic monolayer has the strongest affinity for the seed nanocrystal.[38] Different methods to prepare ZnO/Fe_xO_y heterodimers have also been reported and their magnetic/luminescent properties were investigated.[39,40] Cozzoli et al. synthesized binary γ-Fe_2O_3/TiO_2 by heterogeneous nucleation of iron oxide onto the longitudinal facets of anatase TiO_2 nanorods in a ternary surfactant mixture and described their mechanism of formation.[41,42] Tremel and co-workers recently reported the synthesis of core/shell and heterodimer $Cu@Fe_3O_4$ nanoparticles using Cu(II) acetate and $Fe(CO)_5$ as organometallic reagents.[43] However, information about the reaction yield, the extent of oxidation of the Cu component, and the electronic properties of the particles was not provided.

Here we report the synthesis of γ-Fe_2O_3/Cu_2O HNCs by a solution-phase seeded growth approach and investigate their structure, composition, and electronic band alignment by X-ray/UV photoelectron spectroscopy (XPS/UPS). γ-Fe_2O_3 is a metastable, ferrimagnetic n-type semiconductor possessing the same inverse spinel structure as magnetite (Fe_3O_4) but with Fe (II) vacancies in the octahedral sites. Cu_2O is an intrinsic p-type semiconductor with a bandgap of ~ 2.1 eV.[44] Their natural abundance, low cost and significant visible light absorption has resulted in much effort dedicated to using these materials for photocatalytic and photoelectrochemical H_2 production.[45,46] However, both γ-Fe_2O_3 and Cu_2O suffer from short minority carrier diffusion lengths (<10 nm) and lifetimes (~10 ps).[45] Cu_2O is also known to be susceptible to photocorrosion in aqueous solution.[47] An effective way to address these issues is provided by "bandgap engineering" of heterostructured nanocrystals to manipulate photogenerated charge

dynamics.[48] When the bands of adjacent material domains form a staggered alignment across the heterojunction, spatial separation of charge carriers within the heterostructure is promoted thereby localizing the electronic wavefunction on one component, with the hole wavefunction residing on the other domain.[48] This is referred to as a type II band alignment and is reported to result in reduced overlap of electron and hole wavefunctions leading to longer excited state lifetimes and more charge carriers available to perform useful functions such as participating in redox reactions with surface-adsorbed reactants.[48] This work is an attempt to determine whether the above strategy could be applicable to two of the most promising functional oxides intended for use in solar energy conversion.

2. EXPERIMENTAL SECTION

Chemicals. Iron trichloride ($FeCl_3 \cdot 6H_2O$, 97%), sodium oleate (82% fatty acid basis) Cu(I) acetate 97%, trioctylamine (TOA, 98%), 1-octadecene (ODE, tech. 90%), oleic acid (OA, tech. 90%), iron (II) oxide nanopowder, iron (II,III) oxide nanopowder, and anhydrous organic solvents were purchased from Sigma Aldrich and used without further purification.

Synthesis Procedures. All synthetic manipulations were done using standard airless techniques. Fe-oleate was synthesized according to a previously reported procedure.[49] Iron trichloride (4.32 g, 16.0 mmol) and sodium oleate (14.6 g, 48 mmol), were dissolved in 110 mL of 4:3:7 ethanol:water:hexane mixture and refluxed at 70°C under Ar for 4 hours. The solution was cooled to room temperature; the upper organic layer was separated and washed twice with 20 mL distilled water. Solvent was removed on a rotary evaporator giving a viscous deep red liquid. The product was dried at 70°C in a vacuum oven for 48 hours, resulting in $Fe(oleate)_3$ in the form of a waxy red solid.

γ-Fe₂O₃ Nanocrystals – γ-Fe$_2$O$_3$ nanocrystals used as seeds in the synthesis of HNCs were prepared according to a modified literature procedure.[49] 2g Fe(oleate)$_3$, 14 mL 1-octadecene, and 0.35 mL oleic acid were added to a 100 mL 2-neck round bottom flask and heated to ~60°C for 10 minutes to solubilize Fe(oleate)$_3$. Using a spherical heating mantle, the reaction mixture was heated to 320°C over the course of 20 minutes at an average rate of 13°C per minute, under Ar flow. The temperature was maintained at 320°C for 30 minutes, after which the reaction mixture was cooled to room temperature and 5 mL toluene added. The nanocrystals were precipitated by addition of excess EtOH, centrifuged at 7800 rpm for 20 minutes, and redispersed in heptane. Two redispersion/precipitation cycles were performed to remove excess Fe(oleate)$_3$.

Cu@Cu₂O Nanocrystals – Cu@Cu$_2$O core-shell nanocrystals were prepared according to a modified literature procedure.[51] 0.245g Cu(I) acetate, 7.5 mL trioctylamine, and 2 mL oleic acid were added to a 50 mL 3-neck round bottom flask in a N$_2$-filled glovebox. The flask was connected to a Schlenk line and degassed under vacuum at 60°C for at least 30 minutes. The flask was then filled with Ar, heated to 180°C at a rate of 12°C per minute, and kept at that temperature for 45 minutes. The reaction mixture was then heated to 270°C at 10°C resulting in a color change to deep burgundy indicative of nucleation of elemental Cu. Particle growth was continued at 270°C for 45 minutes. The mixture was then cooled to room temperature, 5 mL of toluene was added and the particles were precipitated by centrifugation in excess EtOH at 7800 rpm for 20 minutes, followed by redispersion in heptane. Complete oxidation to Cu$_2$O was observed within 48 hours upon storage in air.

γ-Fe₂O₃/Cu₂O HNCs – The γ-Fe$_2$O$_3$ seeds were synthesized as described above but the particles were not isolated. Instead, following 30 minutes at 320°C, the reaction mixture was

cooled to 150°C, at which point a degassed, 60°C solution of 0.123 g Cu(I) acetate, 7.5 mL trioctylamine, and 2 mL oleic acid was rapidly injected via metal syringe resulting in a temperature decrease to ~ 120°C. The mixture was then rapidly heated back to 150°C and particle growth was continued for 15-60 minutes. After the completion of the growth period, the flask was cooled to room temperature, 5 mL toluene was added, and the HNCs were precipitated by centrifugation in excess EtOH at 7800 rpm for 20 minutes, followed by redispersion in heptane. Three redispersion/precipitation cycles were performed to remove unreacted starting material and free ligand.

Characterization. TGA curves were acquired on a TA Instruments Q500 thermogravimetric analyzer at a constant ramp rate of 5°C under N_2 atmosphere. UV-VIS absorption spectra were recorded on a Perkin Elmer Lambda 900 UV/VIS/NIR spectrophotometer in dilute heptane solutions. NMR spectra of the precursors were acquired on a Varian Mercury 400 MHz spectrometer in $CDCl_3$.

Electron Microscopy. Low resolution TEM images were acquired on a Hitachi H-7000 conventional TEM operating at 100kV. HRTEM images and STEM EELS spectra were acquired on a Hitachi H-3300 ETEM, a JEOL JEM 2010 operating at 200kV and a Nion UltraSTEM100 operated at 100 kV and equipped with a Gatan Enfina spectrometer. Sample preparation involved dropping a dilute nanocrystal solution on a carbon coated Ni TEM grid. EDX analysis was performed on a Hitachi S-5200 SEM operating in TEM mode using an Oxford Inca detector. Particle size and yield determination was done manually using the free ImageJ software on a minimum of 200 particles.

Powder X-Ray Diffraction. Powder X-ray diffraction patterns were recorded on Siemens D5000 and Bruker D2 Phaser instruments using CuKα line as excitation source. Samples were prepared by drop-casting a concentrated nanocrystal solution onto Si(100) substrates to give films of at least 1 micrometer in thickness.

Raman Spectroscopy. Raman spectra were measured in backscattering configuration utilizing a 532nm solid-state laser, Tornado Hyperflux U1 spectrometer, and a cooled CCD detector. The spectral resolution was 5 cm^{-1} and the beam size on the sample was 10 microns. The laser power was 0.5 mW to avoid laser induced transition of γ-Fe_2O_3 to alpha-Fe_2O_3. Raman analysis samples were prepared by drop-casting concentrated nanocrystal solutions onto a silica glass substrate to give a film of at least 1 micrometer in thickness.

Photoelectron Spectroscopy. XPS/UPS spectra were acquired using a PHI 5500 instrument. An Aluminum K-alpha light source with X-ray wavelengths of 1486.7 eV under UHV conditions (< 1 x 10^{-9} Torr) was used for XPS spectra. Photons with energy of 21.22 eV generated by helium plasma with a back pressure of 2 x 10^{-5} Torr were used for UPS spectra. A beam of Xenon ions with kinetic energy of 3.0 eV was used to sputter-clean the sample surface of organic ligand prior to analysis. Sputtering was performed for an average of three minutes corresponding to a sputtering depth of ~ 2nm. Samples for XPS/UPS analysis were prepared by drop-casting dilute nanocrystal solutions on p-doped Si(100) substrates to give a film of ~50 nm thickness. The substrates were cleaned of organics by immersion into 3:1 $NH_4OH:H_2O_2$ solution at 50°C for 12 hours prior to film formation.

3. RESULTS AND DISCUSSION

3.1 Synthesis and Electron Microscopy

The present synthetic pathway uses γ-Fe$_2$O$_3$ nanocrystals as seeds for the heterogeneous nucleation of metallic Cu followed by oxidation of the Cu domain to Cu$_2$O upon post-synthetic exposure to air to form γ-Fe$_2$O$_3$/Cu$_2$O hetero-structured nanocrystals. The γ-Fe$_2$O$_3$ seeds were prepared by thermal decomposition of Fe(oleate)$_3$ precursor in 1-octadecene at 320°C according to a modified literature procedure.[49] Fe(oleate)$_3$ was synthesized from FeCl$_3$·6H$_2$O and sodium oleate in a biphasic reaction mixture and its structure confirmed by ^{1}H NMR and IR spectroscopy (see Figures S1&S2). Thermogravimetric analysis (TGA) of Fe(oleate)$_3$ (see Figure S3) indicated a loss of the first oleate ligand at 200°C followed by loss of the remaining two at 320°C in agreement with literature.[50] The bare γ-Fe$_2$O$_3$ nanocrystals display cubic and spherical morphologies and are 12.6 ± 1.5nm in diameter (see Figure S4). The Cu@Cu$_2$O particles were synthesized according to a modified literature procedure by reduction of Cu(I) acetate with trioctylamine at 270°C followed by post-synthetic oxidation to Cu$_2$O upon exposure to air.[51] The copper component of the HNCs was introduced by lowering the injection temperature of the Cu(I) acetate precursor solution to 150°C and allowing for a period of growth ranging from 15 to 60 minutes. It is interesting to note that nucleation of metallic Cu is observed at the significantly lower temperature of 150°C in the HNC synthesis as compared to 250°C when the bare Cu@Cu$_2$O were made without pre-existing γ-Fe$_2$O$_3$ seeds in solution. This is consistent with heterogeneous nucleation being more thermodynamically favorable than homogeneous nucleation[5,7] and suggests that γ-Fe$_2$O$_3$/Cu$_2$O HNCs form by a seeded growth mechanism. TGA

scans of the Cu(I) acetate precursor (see Figure S3) confirm its decomposition temperature in the range of 120-160°C consistent with the above observation. Attempts to carry out the Cu(I) acetate reduction reaction on pre-formed γ-Fe$_2$O$_3$ seeds did not result in HNC formation indicating that Cu nucleation can only occur *in-situ*. This suggests that the presence of an oxygen deficient iron oxide phase may be responsible for chemically reducing the Cu^{+1} precursor to Cu^0 with simultaneous oxidation of iron sites to Fe^{3+} upon exposure to air.
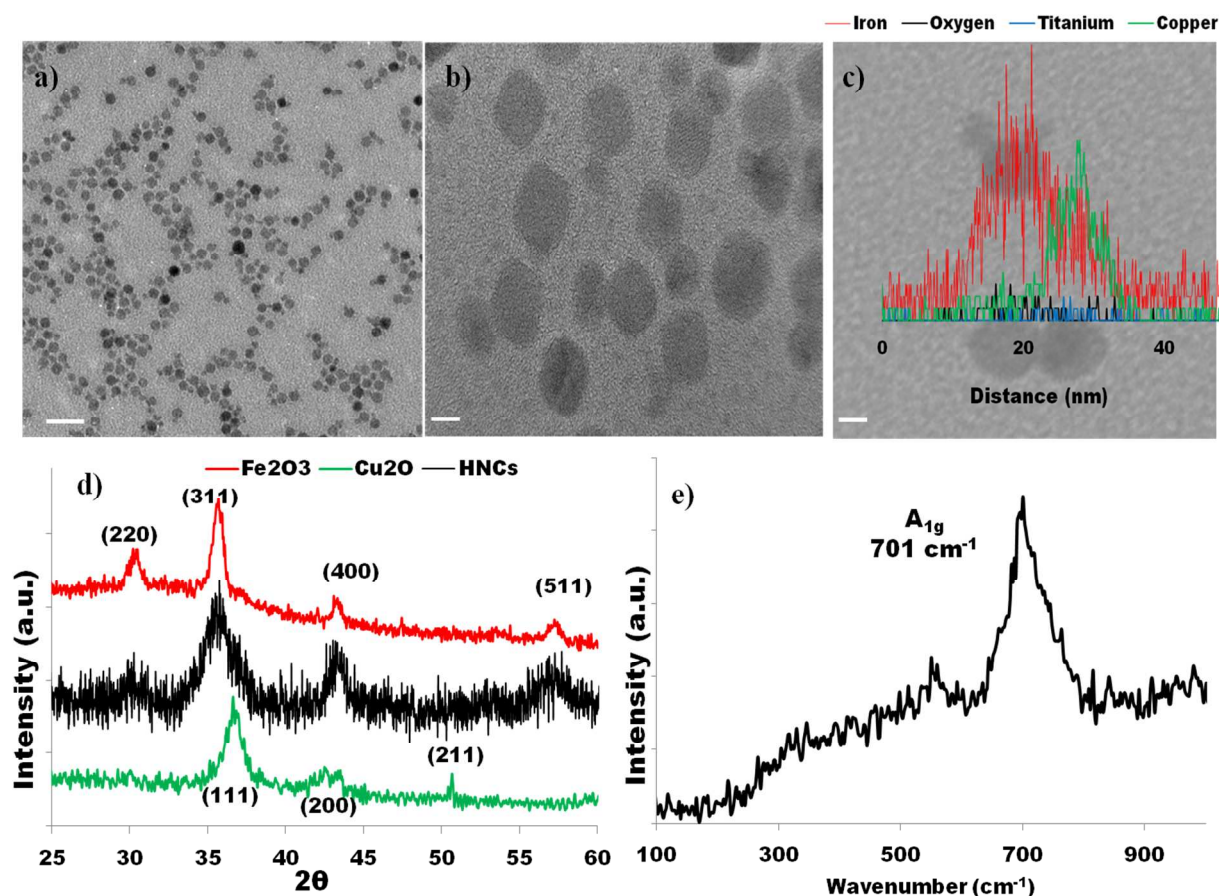
Figure 1. a) Representative low resolution bright-field TEM image of as synthesized HNCs (scale bar is 20 nm) **b)** HRTEM image showing isolated, dimer, and trimer morphologies (scale bar is 5nm) **c)** EDX line scan across dimer particle showing the Fe-rich and Cu-rich domains (the spectra are shifted up for clarity, scale bar 5 nm). **d)** PXRD patterns of Cu$_2$O, γ-Fe$_2$O$_3$, and γ-

Fe$_2$O$_3$/Cu$_2$O HNCs as thin films on a Si wafer. **e)** Raman spectrum of as-synthesized γ-Fe$_2$O$_3$ nanocrystals showing the prominent A$_{1g}$ phonon mode at 701 cm^{-1} indicative of γ-Fe$_2$O$_3$.

Figure 1 shows representative TEM images of the resulting HNCs (Figure 1a,b). Three distinct particle morphologies are observed including isolated seeds, γ-Fe$_2$O$_3$/Cu$_2$O heterodimers, and higher oligomers consisting mainly of Cu$_2$O/γ-Fe$_2$O$_3$/Cu$_2$O heterotrimers. The γ-Fe$_2$O$_3$ component of the HNCs has an average diameter of 11.6 ± 1.4 nm in agreement with the isolated iron oxide particles. In contrast, the Cu$_2$O components are significantly smaller with average diameters of 8.2 ± 1.9 nm and 7.1 ± 1.3 nm in the dimers and oligomers respectively as compared to 13.8 ± 2.6 nm in the isolated particles (see Figure S5). Control experiments were performed to confirm that the HNC architecture was not a result of post-synthetic assembly (see Figure S6). A physical mixture of Cu$_2$O and γ-Fe$_2$O$_3$ particles did not exhibit spontaneous ordering into hetero-nanocrystals suggesting that the observed dimer and oligomer architectures are a result of seeded growth of Cu on γ-Fe$_2$O$_3$ in solution. To confirm that the particles consist of distinct iron and copper-containing domains we performed energy-dispersive X-ray analysis (EDX) on the HNCs as shown in Figure 1c. The resulting spectra are overlaid with the TEM image of the examined particle, which shows the Fe and Cu signals corresponding to separate iron (left) and copper oxide (right) domains. The powder X-ray diffraction patterns of the pure iron oxide and copper oxide particles and the HNCs are shown in Figure 1d. The prominent Cu$_2$O (111) reflection and the absence of metallic Cu reflections indicate fully oxidized Cu$_2$O particles. The pure iron oxide particles exhibit reflections assigned to an inverse spinel structure, either Fe$_3$O$_4$ or γ-Fe$_2$O$_3$. This is typically the case in solution phase syntheses which are limited by the boiling points of common solvents. Formation of the thermodynamically stable α-Fe$_2$O$_3$ requires temperatures above 400°C. The Fe$_3$O$_4$ and γ-Fe$_2$O$_3$ polymorphs cannot be distinguished

by PXRD because they have very similar crystal structures, with the only difference being the presence of Fe(II) vacancies in the octahedral site of the gamma phase. Therefore, Raman spectroscopy was used to distinguish between these phases as has been reported previously.[27] Pure Fe_3O_4 exhibits a A_{1g} phonon mode at ~ 670 cm^{-1} which broadens and shifts to ~700 cm^{-1} as the sample is oxidized to γ-Fe_2O_3.[27,52] The Raman spectrum of the pure iron oxide nanocrystals is shown in Figure 1e with the A_{1g} mode present at 701 cm^{-1} suggesting that the iron oxide component is mainly γ-Fe_2O_3. The PXRD spectrum of the HNCs in Figure 1c exhibits broadened reflections corresponding to γ-Fe_2O_3. The Cu_2O reflections are not apparent likely due to their lower abundance, smaller size and a low signal-to-noise ratio caused by X-ray fluorescence from the γ-Fe_2O_3 component.
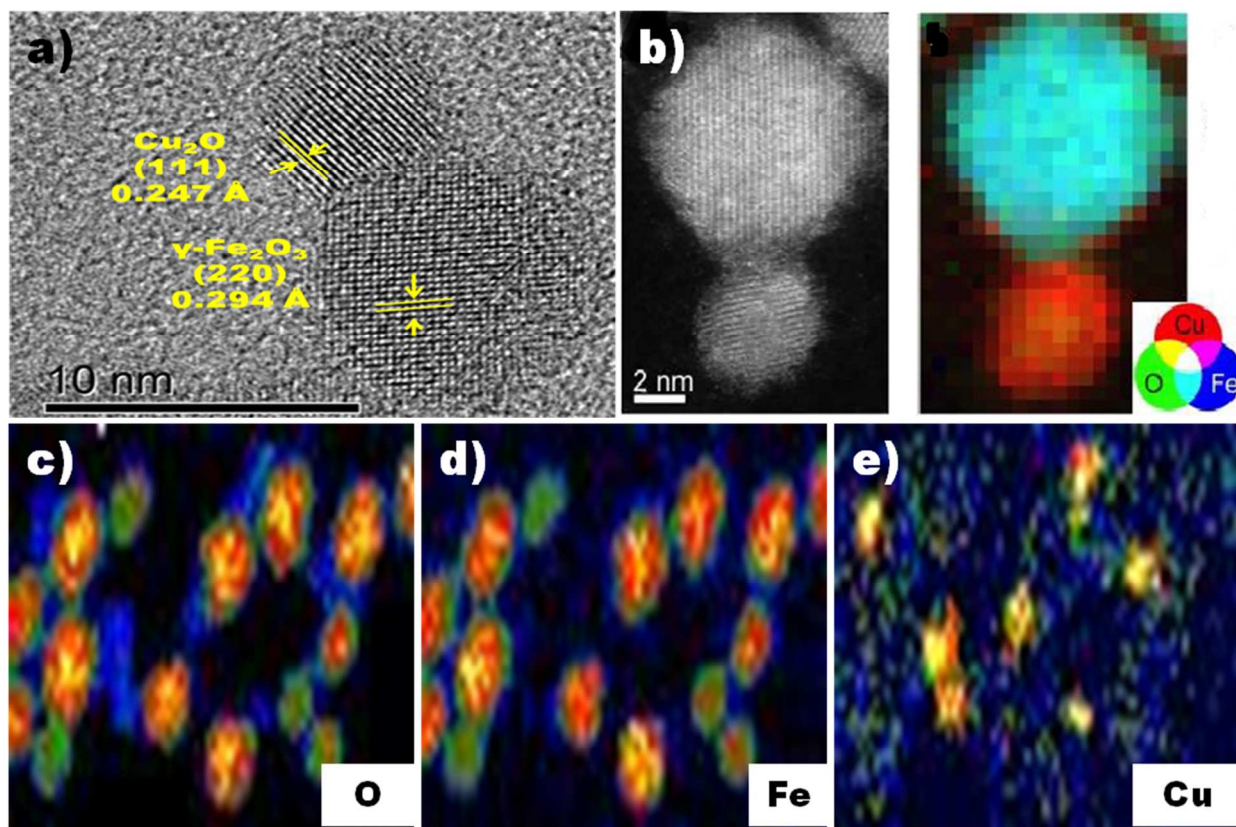
Figure 2. a) HRTEM image of the γ-Fe_2O_3/Cu_2O nanocrystals showing the Cu_2O (111) and γ-

Fe$_2$O$_3$ (220) lattice planes **b)** HR-STEM image and STEM-EELS elemental map obtained from the Cu $L_{2,3}$ (red), Fe $L_{2,3}$ (blue), and O K (green) edges, showing the compositional distribution of a single heterodimer. Data acquired in an aberration corrected Nion UltraSTEM100 operated at 100 kV. **c-e)** STEM-EELS elemental map of Cu, Fe, and O domains showing the compositional distribution over a larger area. The color of the image is proportional to signal intensity with red indicating the strongest signal and blue the weakest.

Figure 2a shows a high resolution TEM image of a single γ-Fe$_2$O$_3$/Cu$_2$O dimer. The lattice spacing of the two domains were measured to be 0.247 Å and 0.294 Å corresponding to the (111) and (220) planes of Cu$_2$O and γ-Fe$_2$O$_3$ respectively. Figure 2b-e show electron energy loss spectroscopy (EELS) elemental maps tracing the compositional distribution of a single dimer and over a larger area. The Fe and O signals overlap perfectly giving the location of the γ-Fe$_2$O$_3$ seeds. The Cu-containing domains are clearly visible adjacent to the predominant γ-Fe$_2$O$_3$ nanocrystals. The O content of the Cu$_2$O domains is also confirmed by the blue regions in Figure 2c, confirming their oxidation from metallic Cu to Cu$_2$O.
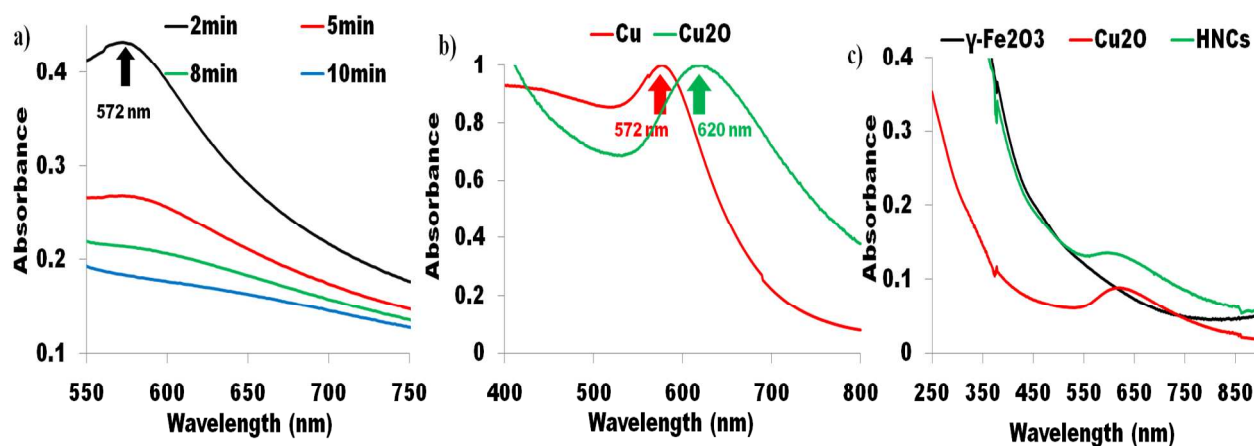
Figure 3. UV-VIS optical absorbance spectra of **a)** Cu_2O nanocrystals showing initial Cu d-d transition up to 10 min after exposure to air **b)** Cu_2O excitonic absorption after 24 hour exposure to air and **c)** γ-Fe_2O_3, Cu_2O, and γ-Fe_2O_3/Cu_2O HNCs.

3.2 UV-Vis and Reaction Optimization

The optical properties of the HNCs are presented in Figure 3. Initially the dominant feature in the optical spectrum is a Cu d-d transition at 572 nm which rapidly decreases in intensity as a result of oxidation in air, Figure 3a.[53] After allowing oxidation to proceed for 24 hours, the appearance of a new feature at 620 nm is observed, Figure 3b. This spectral signature is attributed to the excitonic transition of Cu_2O in the range of 2.0-2.2 eV.[54] The UV-VIS spectra of pure γ-Fe_2O_3, the fully oxidized Cu_2O component and the HNCs are shown in Figure 3c. The HNC spectrum shows features of both constituent spectra including the Cu_2O transition and the tail into the UV characteristic of γ-Fe_2O_3.
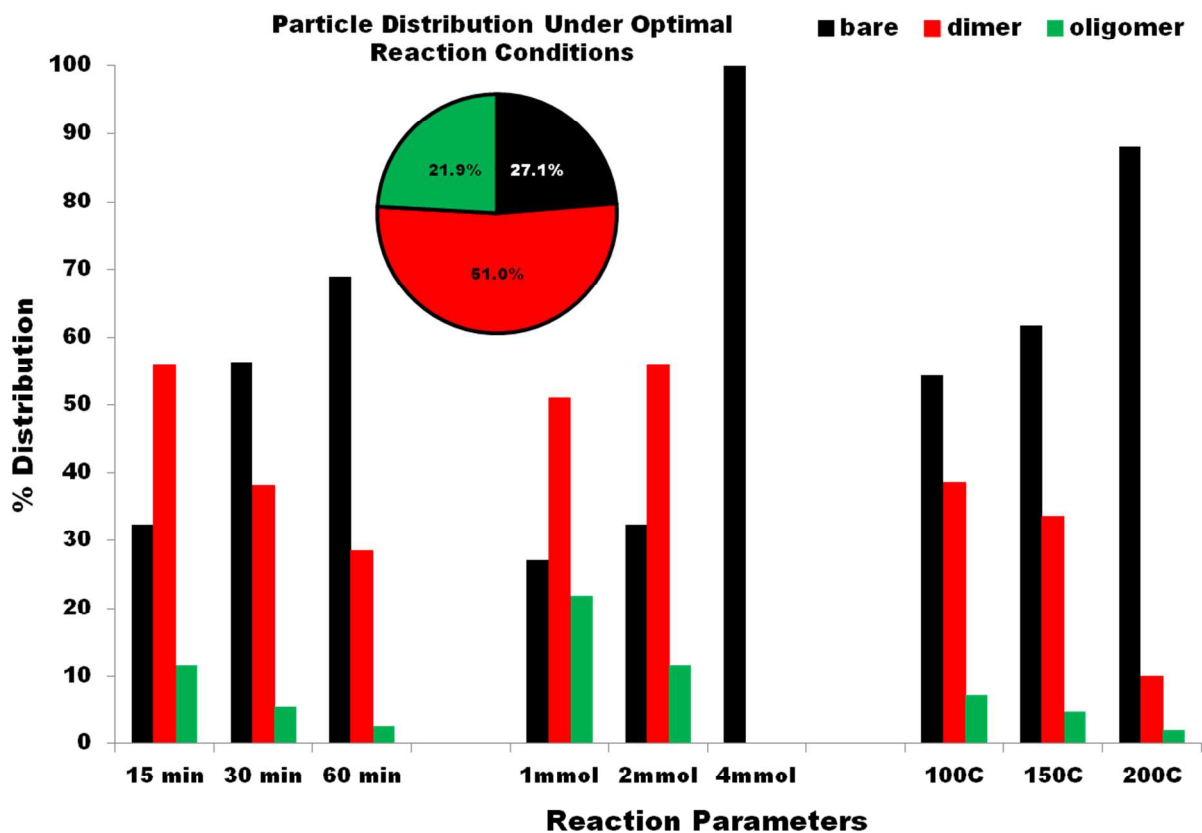
Figure 4. % Distribution of isolated, dimer, and oligomer particles as a function of reaction, time, temperature, and stoichiometry. Inset: Reaction yield under optimal conditions of 15min, 150°C, and 1 mmol Cu(I) acetate precursor.

We then examined the effect of varying the reaction parameters in an attempt to maximize the yield of HNCs with respect to isolated particles. Figure 3 shows the percentage particle distribution as a function of varying the reaction time, stoichiometry, and Cu precursor injection temperature. In determining the yield of HNCs we consider the proportion of dimers and higher oligomers in the total particle count. Increasing the growth time at a fixed temperature of 150°C leads to a decrease in the yield of HNCs from a total of ~65% to just over 30%. This is likely caused by thermal de-attachment of the Cu component from the seeds upon prolonged heating. The injection temperature of the Cu(I) acetate precursor also has an effect on HNC yield

as seen in the right side of Figure 4. The HNC yield decreases on increasing the injection temperature from 100°C to 150°C, and 200°C. This effect is consistent with previous knowledge in the field of hetero-nanocrystal synthesis; heterogeneous nucleation is facilitated by the seed surface thereby lowering the activation energy for nucleation.[5] However, using an injection temperature of 100°C resulted in some colloidally unstable byproduct of bulk Cu_2O which had to be removed before the yield was determined. When the reaction was repeated at 150°C, no bulk byproduct was observed and therefore 150°C was identified as the optimal injection temperature despite giving a slightly lower HNC yield than the 100°C reaction. Varying the amount of Cu(I) acetate precursor in the range of 1,2, and 4 mmol while holding the growth time (15min), temperature (150°C) and amount of Fe(oleate)$_3$ (2mmol) constant also had an effect on the yield. We found that using 1 mmol of Cu(I) acetate (2:1 Fe:Cu molar ratio) results in higher HNC yield than when a 1:1 Fe:Cu ratio was employed. This is likely caused by incomplete decomposition of Fe(oleate)$_3$, as evidenced by unreacted precursor that had to be removed by centrifugation post-synthesis. Increasing the Cu(I) acetate amount to 4 mmol resulted exclusively in isolated γ-Fe_2O_3 particles and bulk Cu_2O precipitate. Under the optimal reaction conditions identified in Figure 3, an HNC yield of 72% was achieved, consisting of approximately 51% heterodimers and 21% trimers and higher oligomers. Upon size-selective precipitation with ethanol, the trimers and larger oligomers can essentially be removed from solution leading to fractions that are enriched in dimers with a corresponding amount of remaining isolated γ-Fe_2O_3 particles (see Figure S7).
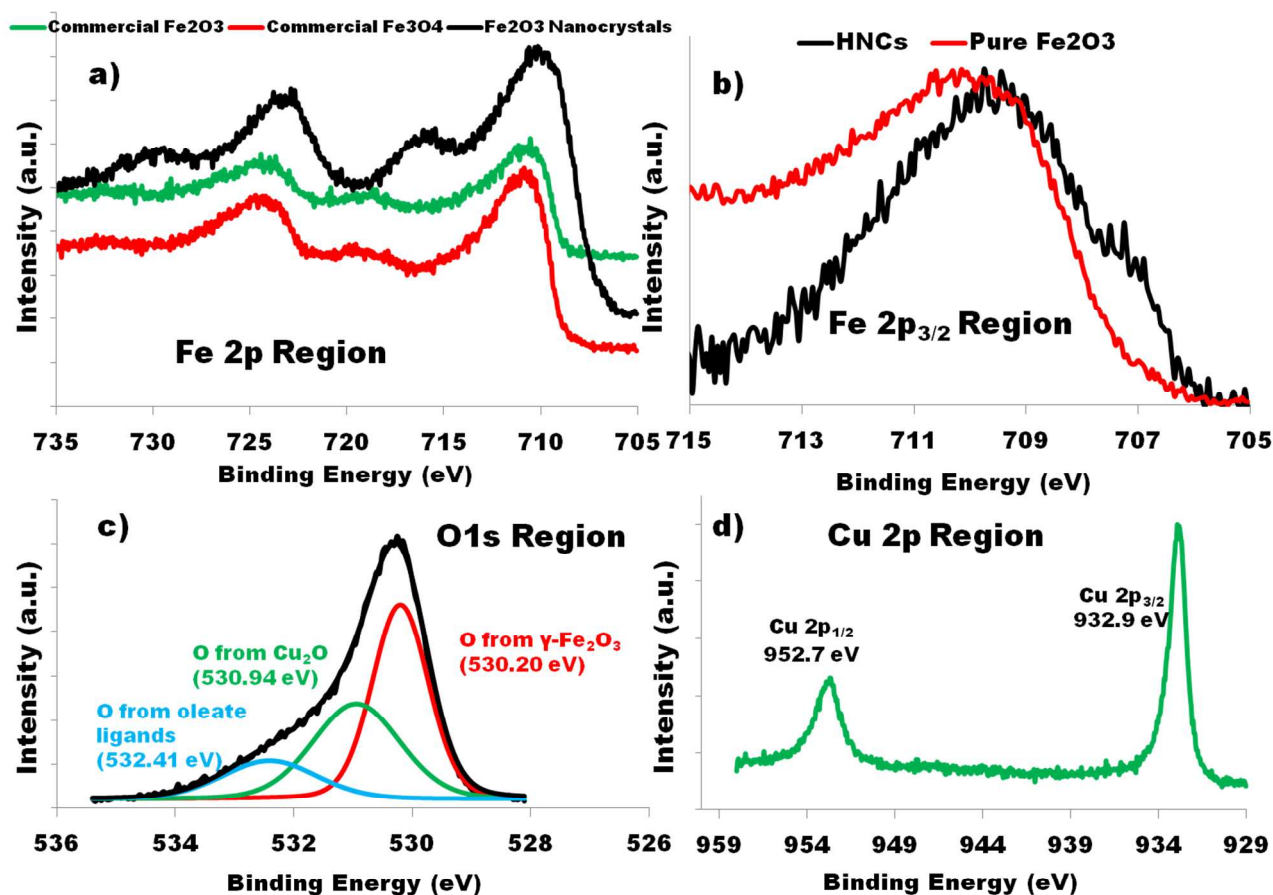
Figure 5. a) XPS spectra of Fe 2p core-level lines of commercial γ-Fe$_2$O$_3$ and Fe$_3$O$_4$ powders, and the as-synthesized γ-Fe$_2$O$_3$ nanocrystals **b)** XPS spectrum of the Fe2p$_{3/2}$ region of the HNCs and isolated γ-Fe$_2$O$_3$ nanocrystals **c)** XPS spectrum of the HNCs O1s region with peak fitting i) O signal from γ-Fe$_2$O$_3$ ii) O signal from Cu$_2$O iii) O signal from carboxylate ligand **d)** XPS spectrum of the HNCs Cu 2p region.

3.3 X-ray and Ultraviolet Photoelectron Spectroscopy

In order to fully determine the chemical and electronic properties of γ-Fe$_2$O$_3$/Cu$_2$O HNCs we performed an X-ray/ultraviolet photoelectron spectroscopy (PES) study of our materials. PES is a useful, non-destructive tool for studying the chemical and electronic structure of

nanocrystalline samples as it can provide information about elemental composition, oxidation state, and density of states near the Fermi level.[55] The presence of both Cu and Fe in the HNCs was confirmed by the characteristic Fe and Cu 2p doublets in the XPS survey scans (see Figure S8). We further employed XPS to ascertain that the iron oxide component of our HNCs was indeed γ-Fe_2O_3 as determined by Raman spectroscopy. XPS has previously been used to differentiate between Fe_2O_3 and Fe_3O_4 based on the difference in binding energy between Fe^{2+} and Fe^{3+}.[56,57] Figure 5a shows the Fe 2p core-level peaks of the as-synthesized pure iron oxide nanocrystals and commercial γ-Fe_2O_3 and Fe_3O_4 nanopowders analyzed under the same conditions. The binding energies of the Fe $2p_{1/2}$ and Fe $2p_{3/2}$ peaks are summarized in Table 1 which indicates that the nanocrystalline iron oxide lines closely correspond to the commercial γ-Fe_2O_3 powder thereby confirming our assignment.

Table 1. Binding Energy (eV) of Fe 2p core-level lines in γ-Fe_2O_3 nanocrystals, γ-Fe_2O_3/Cu_2O HNCs, and commercial iron oxide nanopowders.

Sample	Fe $2p_{3/2}$	Fe $2p_{1/2}$
γ-Fe_2O_3 Nanocrystals	710.2 eV	723.9 eV
γ-Fe_2O_3 /Cu_2O HNCs	709.4 eV	723.0 eV
Commercial γ-Fe_2O_3 Nanopowder	710.6 eV	724.4 eV
Commercial Fe_3O_4 Nanopowder	710.9 eV	724.8 eV

The Fe $2p_{3/2}$ region of the HNCs is shown in Figure 5b. The main peak is shifted to a lower binding energy of 709.4 eV, as a result of the presence of the Cu_2O domain. A small

shoulder at 706.9 eV is also present which may be assigned to Fe^0 likely at the interfacial junction region. Figure 5c shows the O1s region of the HNCs. The peak can be de-convoluted into three component peaks corresponding to oxygen in Fe_2O_3 and Cu_2O environments, and the carboxylic group of surface oleate ligands, in agreement with database values. Finally, the Cu 2p region of the HNCs is shown in Figure 5d. The Cu $2p_{3/2}$ and $2p_{1/2}$ lines are present at 932.9 and 952.7 eV respectively, consistent with Cu^+ literature values.[51] In contrast to O'Brien et. al. we did not observe any satellite peaks in the range of 934-940 eV that would indicate a CuO layer on the Cu_2O surface.[51]

The electronic structure of hetero-nanocrystals is of particular interest with respect to using these materials in photocatalysis or photovoltaics. Using ultraviolet photoelectron spectroscopy we probed the density of states near the Fermi level, which allows extraction of the Fermi energy and valence band (VB) maximum. Figure 6a shows the secondary electron cutoff peak of our materials, which allows the determination of the work function and Fermi level. The HNC sample's valence band maximum (VBM) is found between the two isolated components suggesting electronic contact between the two domains. A physical mixture of the two isolated nanocrystals was also evaluated. In such a mixture there is no electronic contact between the two components and UPS will only detect electrons with the lowest kinetic energy corresponding to the γ-Fe_2O_3 component in our system. Figure 6a shows that the secondary electron cutoff edge of the physical mixture spectrum overlaps that of the γ-Fe_2O_3. The valence photoemission spectra in Figure 6b allow determination of the VBM energy with respect to the Fermi level. The densities of states of the HNCs originate mostly from the γ-Fe_2O_3 component. The small shoulder at 1.5 eV in the spectra of γ-Fe_2O_3, the HNCs, and the physical mixture corresponds to a Fe^{2+} satellite peak caused by reduction of Fe^{3+} by the sputtering beam. The Cu_2O valence band spectrum

indicates that the valence band electron density extends all the way to Fermi level which is consistent with a fully occupied d band.[55]
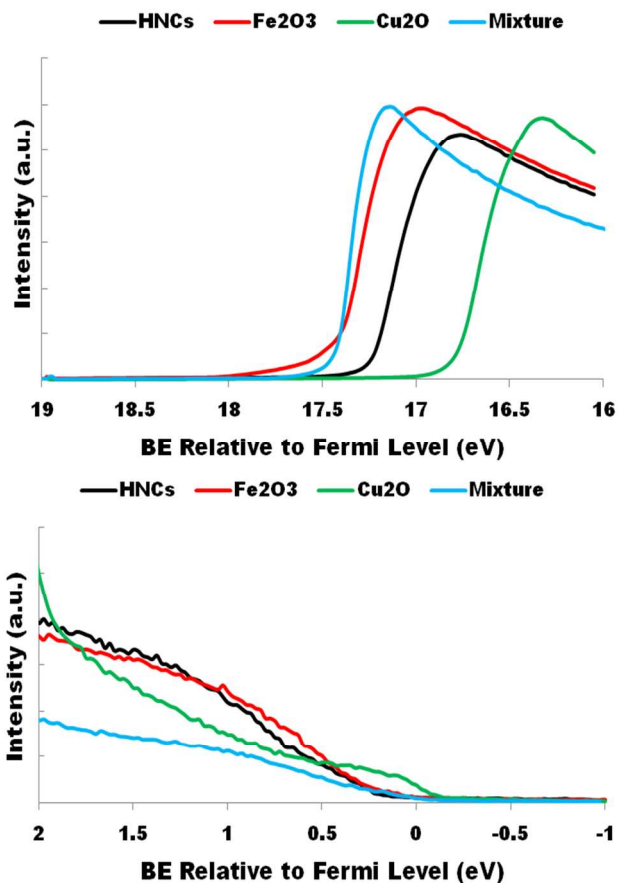
Figure 6. a) The secondary electron cut-off region of the γ-Fe$_2$O$_3$/Cu$_2$O HNCs, their pure components, and the physical mixture of the isolated nanocrystals **b)** Valence band edge photoemission spectra of HNCs and their components

Having determined the position of the valence band maxima of the HNCs and their constituents by UPS, we can construct an electronic band energy diagram as a step towards understanding the charge carrier behavior in our system. Scheme 1 shows the Fermi levels, and conduction and valence band energies of the HNCs, their individual components and

corresponding commercial samples. The positions of the conduction band (CB) minima were calculated by adding the bandgap as determined by UV-VIS spectroscopy (see Figure S9) to the valence band maxima found by UPS.[58]
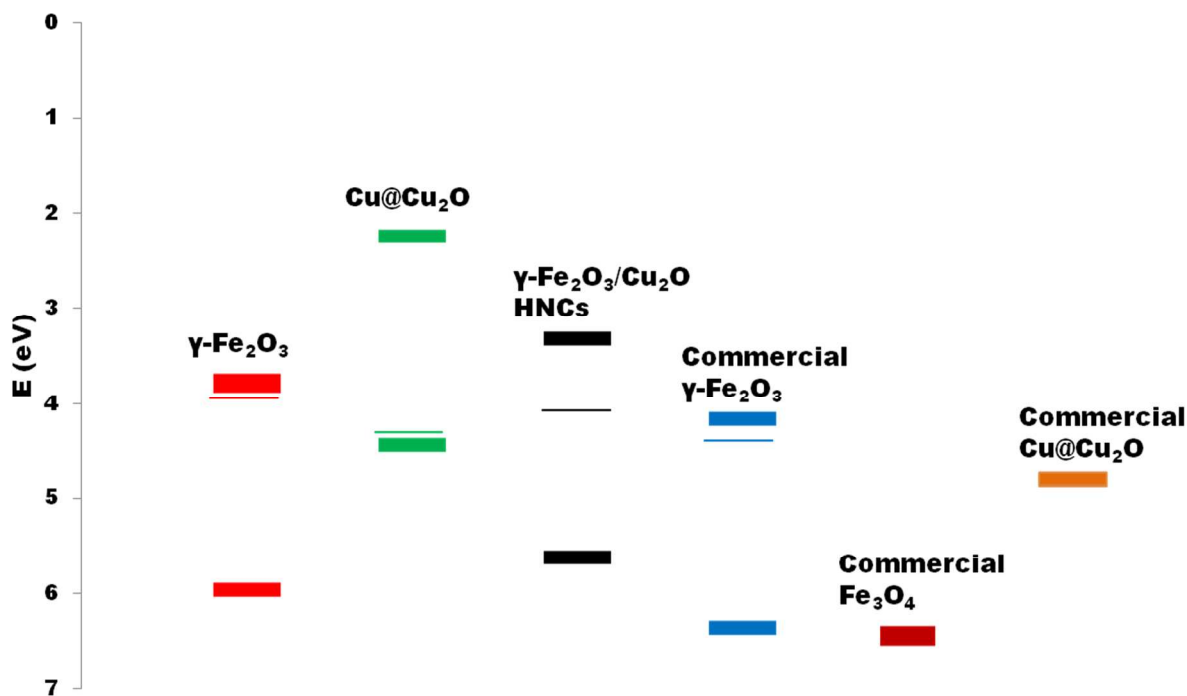
Scheme 1. Band energy diagram showing the valence and conduction band edges and Fermi levels of the HNCs and their constituents. The commercial samples of copper and iron oxides were evaluated under the same conditions for comparison.

The Fermi level and valence band maximum of the HNCs is found to be between those of γ-Fe_2O_3 and Cu_2O pointing to contributions from both components. In agreement with the literature on the bulk materials, we found that γ-Fe_2O_3 and Cu_2O nanocrystals are intrinsically n-doped and p-doped, likely from anion and cation vacancies, respectively. Considering the staggered type II band alignment, a photoexcited electron in the conduction band of Cu_2O would relax to the conduction band of γ-Fe_2O_3, promoting its separation from the hole in the Cu_2O

valence band. Alternatively a two-photon Z-scheme could also be observed where initial excitation of γ-Fe$_2$O$_3$ and relaxation into the VB of Cu$_2$O is followed by absorption of a secondary photon and promotion to its CB analogous to the process in Photosystems I and II.

4. CONCLUSION

We have reported the colloidal synthesis of γ-Fe$_2$O$_3$/Cu$_2$O hetero-nanocrystals by thermal decomposition of Cu(I) acetate on γ-Fe$_2$O$_3$ at 150°C leading to the nucleation of a metallic Cu domain followed by its conversion to Cu$_2$O upon exposure to air. The reduced electron-hole recombination resulting from the type II band alignment formed between the two components renders γ-Fe$_2$O$_3$/Cu$_2$O HNCs potentially useful as photocatalysts for pollutant degradation and solar fuel production. Our work represents an example of targeting a particular HNC functionality by design through judicious selection of its components. In order to accelerate the transition of hetero-nanocrystals from promise to utility, we believe that synthetic efforts should move away from proof-of-concept examples involving cadmium and zinc chalcogenides and focus on incorporating materials that have already proven suitable for a particular application. Reproducible synthetic pathways with high HNC yields are highly desirable, specifically ones incorporating functional oxides such as TiO$_2$, NiO, and WO$_3$.

Supporting Information Available: Additional ^{1}H NMR, IR, UV-VIS spectra, TEM images, TGA scans, and XPS survey scans. This material is available free of charge via the Internet at http://pubs.acs.org.

REFERENCES AND NOTES

1. D.V. Talapin, J.-S. Lee, M.V. Kovalenko, and E.V. Shevchenko, *Chem. Rev.* 2010, **110**, 289-458.

2. E.H. Sargent, *Nat. Photon.* 2009, **3**, 325-331.

3. B.Y.S. Kim, J.T. Rutka, and W.C.W. Chan, *N.Engl. J. Med.* 2010, **363**, 2434-2443.

4. X. Chen, S. Shen, L. Guo, and S.S. Mao, *Chem. Rev.* 2010, **110**, 6503-6570.

5. C. De Mello Donega, *Chem. Soc. Rev.* 2011, **40**, 1512-1546.

6. P.D. Cozzoli, T. Pellegrino, and L. Manna, *Chem. Soc. Rev.* 2006, **35**, 1195-1208.

7. L. Carbone, and P.D. Cozzoli, *Nano Today* 2010, **5**, 449-493.

8. R. Costi, A.E. Saunders, and U. Banin, *Angew. Chem. Int. Ed.* 2010, **49**, 4878-4897.

9. P. Reiss, M. Protiere, and L. Li, *Small*, 2009, **2**, 154-168.

10. D. Wang, and Y. Li, *Adv. Mater.* 2011, **23**, 1044-1060.

11. A.E. Saunders, I. Popov, and U. Banin, *J. Phys. Chem. B* 2006, **110**, 25421-25429.

12. D.V. Talapin, J.H. Nelson, E.V. Shevchenko, S. Aloni, B. Sadtler, and A.P. Alivisatos, *Nano Lett.* 2007, **7**, 2951-2959.

13. J. Maynadie, A. Salant, A. Falqui, M. Respaud, E. Shaviv, U. Banin, K. Soulantica, and B. Chaudret, *Angew. Chem. Int. Ed.* 2009, **48**, 1814-1817.

14. L. Zhang, D.A. Blom, and H. Wang, *Chem. Mater*. 2011, **23**, 4587-4598.

15. J. Jiang, H. Gu, H. Shao, E. Devlin, G.C. Papaefthymiou, and J.Y. Ying, *Adv. Mater.* 2008, **20**, 4403-4407.

16. H. Yu, M. Chen, P.M. Rice, S.X. Wang, R.L. White, and S. Sun, *Nano Lett.* 2005, **5**, 379-382.

17. D. Gerion, F. Pinaud, S.C. Williams, W.J. Parak, D. Zanchet, S. Weiss, and A.P. Alivisatos, *J. Phys. Chem. B* 2001, **105**, 8861-8871.

18. M. Liong, J. Lu, M. Kovochich, T. Xia, S.G. Ruehm, A.E. Nel, F. Tamanoi, and J.I. Zink, *ACS Nano* 2008, **2**, 889-896.

19. K.S. Lee, R.M. Anisur, K.W. Kim, W.S. Kim, T.-J. Park, E.J. Kang, and I.S. Lee, *Chem. Mater.* 2012, **24**, 682-687.

20. H. Zhu, and T. Lian, *Energy Environ. Sci.* 2012, **5**, 9406-9418.

21. T. O'Connor, M.S. Panov, A. Mereshchenko, A.N. Tarnovsky, R. Lorek, D. Perera, G. Diederich, S. Lambright, P. Moroz, and M. Zamkov, *ACS Nano* 2012, **6**, 8156-8165

22. O. Chen, J. Zhao, V.P. Chauhan, J. Cui, C. Wong, D.K. Harris, H. Wei, H.-S. Han, D. Fukumura, R.K. Jain, and M.G. Bawendi, *Nat. Mater.* 2013, **12**, 445-451.

23. D.V. Talapin, A.L. Rogach, A. Kornowski, M. Haase, and H. Weller, *Nano Lett.* 2001, **1**, 207-211.

24. T. Mirkovic, D. Rossouw, G.A. Botton, and G.D. Scholes, *Chem. Mater.* 2011, **23**, 181-187.

25. J. Zhang, Y. Tang, K. Lee, and M. Ouyang, *Nature*, 2010, **466**, 91-95.

26. K.-W. Kwon, and M. Shim, *J. Am. Chem. Soc.* 2005, **127**, 10269-10275.

27. K.-W. Kwon, B.H. Lee, and M. Shim, *Chem. Mater.* 2006, **18**, 6357-6363.

28. H. McDaniel, and M. Shim, *ACS Nano* 2009, **3**, 434-440.

29. J. Tang, Z. Huo, S. Brittman, H. Gao, and P. Yang, *Nat. Nanotechnol.* 2011, **6**, 568-572

30. A. Kubacka, M. Fernandez-Garcia, and G. Colon, *Chem. Rev.* 2012, **112**, 1555-1614.

31. S. Rawalekar, and T. Mokari, *Adv. Energy Mater.* 2013, **3**, 12-27.

32. L. Amirav, and A.P. Alivisatos, *J. Phys. Chem. Lett.* 2010, **1**, 1051-1054.

33. S. Chen, and L.-W. Wang, *Chem. Mater.* 2012, **24**, 3659-3666.

34. M. Casavola, R. Buonsanti, G. Caputo, and P.D. Cozzoli, *Eur. J. Inorg. Chem.* 2008, **6**, 837-854.

35. W. Shi, H. Zeng, Y. Sahoo, T.Y. Ohylchanskyy, Y. Ding, Z.L. Wang, M. Swihart, and P.N. Prasad, *Nano Lett.* 2006, **6**, 875-881.

36. M.R. Buck, J.F. Bondi, and R.E. Schaak, *Nat. Chem.* 2012, **4**, 37-44.

37. S.-H. Choi, H.B. Na, Y.I. Park, K. An, S.G. Kwon, Y. Jang, M. Park, J. Moon, J.S. Son, I.C. Song, W.K. Moon, and T. Hyeon, *J. Am. Chem. Soc.* 2008, **130**, 15573-15580.

38. H. Wu, O. Chen, J. Zhuang, J. Lynch, D. LaMontagne, Y. Nagaoka, and Y. Charles Cao, *J. Am. Chem. Soc.* 2011, **133**, 14327-14337.

39. A. Kostopoulou, F. Thetiot, I. Tsiaoussis, M. Androulidaki, P.D. Cozzoli, and A. Lappas, *Chem. Mater.* 2012, **24**, 2722-2732.

40. W. Chiu, P. Khiew, M. Cloke, D. Isa, H. Lim, T. Tan, N. Huang, S. Radiman, R. Abd-Shukor, M.A. Abd. Hamid, and C. Chia. *J. Phys. Chem. C* 2010, **114**, 8212-8218.

41. R. Buonsanti, V. Grillo, E. Carlino, C. Giannini, F. Gozzo, M. Garcia-Hernandez, M.A. Garcia, R. Cingolani, and P.D. Cozzoli, *J. Am.Chem. Soc.* 2010, **132**, 2437-2464.

42. R. Buonsanti, V. Grillo, E. Carlino, C. Giannini, M.L. Curri, C. Innocenti, C. Sangregorio, K. Achterhold, F.G. Parak, A. Agostiano, and P.D. Cozzoli, *J. Am. Chem. Soc.* 2006, **128**, 16953-16970.

43. B. Nakhjavan, M.N. Tahir, F. Natalio, H. Gao, K. Schneider, T. Schladt, I. Ament, R. Branscheid, S. Weber, U. Kolb, C. Sonnichsen, L.M. Schreiber, and W. Tremel, *J. Mater. Chem.* 2011, **21**, 8605-8611.

44. A.E. Rakhshani, *Solid-State Electronics* 1986, **29**, 7-17.

45. T.K. Townsend, E.M. Sabio, N.D. Browning, and F.E. Osterloh, *Energy Environ. Sci.* 2011, **4**, 4270-4275.

46. Z. Zhang, R. Dua, L. Zhang, H. Zhu, H. Zhang, and P. Wang, *ACS Nano* 2013, **7**, 1709-1717.

47. Y. V. Pleskov, and Y.Y. Gurevich, Photocorrosion and Stability. In *Semiconductor Photoelectrochemistry* Consultants Bureau: New York, 1986 pp 209-225.

48. S.S. Lo, T. Mirkovic, C.-H. Chuang, C. Burda, and G.D. Scholes, *Adv. Mater.* 2011, **23**, 180-197.

49. J. Park, K. An, Y. Hwang, J.-G. Park, H.-J. Noh, J.-Y. Kim, J.-H. Park, N.-M. Hwang, and T. Hyeon, *Nat. Mater.* 2004, **3**, 891-895.

50. N. Bao, L. Shen, W. An, P. Padhan, C.H. Turner, and A. Gupta, *Chem. Mater.* 2009, **21**, 3458-3468.

51. M. Yin, C.-K. Wu, Y. Lou, C. Burda, J.T. Koberstein, Y. Zhu, and S. O'Brien, *J. Am. Chem. Soc.* 2005, **127**, 9506-9511.

52. A.M. Jubb, and H.C. Allen, *ACS Appl. Mater. Interfaces* 2010, **2**, 2804-2812

53. F. Wooten, *Optical Properties of Solids* Academic Press, New York, 1972 pp 63-65

54. K.P. Rice, E.J. Walker, M.P. Stoykovich, and A.E. Saunders, *J. Phys. Chem. C* 2011, **115**, 1793-1799.

55. M.T. Greiner, M.G. Helander, W.-M. Tang, Z.-B. Wang, J. Qiu, and Z. Lu, *Nat. Mater.* 2012, **11**, 76-81.

56. S. Poulin, R. Franca, L. Moreau-Belanger, and E. Sacher, *J. Phys. Chem. C* 2010, **114**, 10711-10718.

57. X. Teng, D. Black, N.J. Watkins, Y. Gao, and H. Yang, *Nano Lett.* 2003, **3**, 261-264.

58. J. Tauc, R. Grigorovici, and R. Vancu, *Phys. Stat. Sol.* 1966, **15**, 627-637.

59. A. Dong, X. Ye, J. Chen, Y. Kang, T. Gordon, J.M. Kikkawa, and C.B. Murray, *J. Am. Chem. Soc.* 2011, **133**, 998-1006.

60. A. Houas, H. Lachheb, M. Ksibi, E. Elaloui, C. Guillard, and J.-M. Herrmann, *Appl. Catal., B.* 2001, **31**, 145-157.